



Upscaling high activity oxygen evolution catalysts based on CoFe_2O_4 nanoparticles supported on nickel foam for power-to-gas electrochemical conversion with energy efficiencies above 80%



Félix Urbain^a, Ruifeng Du^{a,*}, Pengyi Tang^{a,b}, Vladimir Smirnov^c, Teresa Andreu^{a,d}, Friedhelm Finger^c, Nuria Jimenez Divins^e, Jordi Llorca^e, Jordi Arbiol^{b,f}, Andreu Cabot^{a,f}, Joan Ramon Morante^{a,g}

^a IREC, Catalonia Institute for Energy Research, Jardins de les Dones de Negre 1, 08930, Sant Adrià de Besòs, Barcelona, Catalonia, Spain

^b Catalan Institute of Nanoscience and Nanotechnology (ICN2), CSIC and BIST, Campus UAB, Bellaterra, 08193, Barcelona, Catalonia, Spain

^c IEK-5 Photovoltaik, Forschungszentrum Jülich, D-52425, Jülich, Germany

^d Universitat Politècnica de Catalunya, Jordi Girona 1–3, 08034, Barcelona, Catalonia, Spain

^e Institute of Energy Technologies, Department of Chemical Engineering and Barcelona Research Center in Multiscale Science and Engineering, Universitat Politècnica de Catalunya, EEBE, 08019, Barcelona, Spain

^f ICREA, Pg. Lluís Companys 23, 08010, Barcelona, Catalonia, Spain

^g Universitat de Barcelona, Martí i Franquès, 1, 08028, Barcelona, Catalonia, Spain

ARTICLE INFO

Keywords:
 CoFe_2O_4
 Colloidal
 OER
 Solar fuels
 Prototype

ABSTRACT

We investigate cobalt ferrite nanoparticles (NPs) supported on large-scale electrodes as oxygen evolution reaction (OER) catalysts. Colloidal CoFe_2O_4 NPs were loaded on low-cost and high surface area nickel foam (NF) scaffolds. The coating process was optimized for large electrode areas, ensuring a proper distribution of the NPs on the NF that allowed overcoming the electrical conductivity limitations of oxide NPs. We were able to produce CoFe_2O_4 -coated NFs having 10 cm^2 geometric surface areas with overpotentials below 300 mV for the OER at a current density of 50 mA/cm^2 . Such impressively low overpotentials suggested using CoFe_2O_4 NP-based electrodes within a water electrolysis device. In this prototype device, stable operating currents up to 500 mA at remarkably low cell-voltages of 1.62 and 1.53 V, at ambient and 50°C electrolyte temperatures, respectively, were reached during operation periods of up to 50 h. The high electrochemical energy efficiencies reached at 50 mA/cm^2 , 75% and 81% respectively, rendered these devices particularly appealing to be combined with low-cost photovoltaic systems for bias-free hydrogen production. Therefore, CoFe_2O_4 NP-based electrolyzers were coupled to low-cost thin-film silicon solar cells with 13% efficiency to complete a system that afforded solar-to-fuel efficiencies above 10%.

1. Introduction

The development of cost-effective large-scale electrodes for highly active and stable oxygen evolution reaction (OER) catalysis is an essential step toward reaching commercial viable solutions for electrochemical water and CO_2 reduction [1]. The OER is a complex multi-step reaction that starts with an OH coordination or H_2O dissociation step in basic or acidic electrolytes, respectively, to form OH^* , where (*) represents an active site at the surface of the catalyst [2]. OH^* is subsequently decomposed to O^* , which reacts with another adsorbed $\text{H}_2\text{O}/\text{OH}$ to form OOH^* . In a last step OOH^* is deprotonated to O_2 , which is finally released. This complex reaction is kinetically less favored than

the concomitant hydrogen evolution reaction (HER), mainly due to the demanding formation of oxygen double bonds and the associated multi-electron transfer step. Due to its complexity, few catalysts have demonstrated high enough OER activities for commercially relevant application. Commercial electrolysis systems currently rely on expensive and scarce elements such as iridium and ruthenium [3], since alternative low-cost catalysts suffer from unpractical high overpotential losses to provide high enough currents ($> 200 \text{ mA}$), what makes them not competitive with alternative H_2 production pathways [4–6].

In recent years, potentially cost-effective catalysts based on transition metal oxides not relying on Pt-group metals have demonstrated high current water electrolysis at operation voltages below 1.6 V [7,8].

* Corresponding author.

E-mail address: ruifengdu@irec.cat (R. Du).

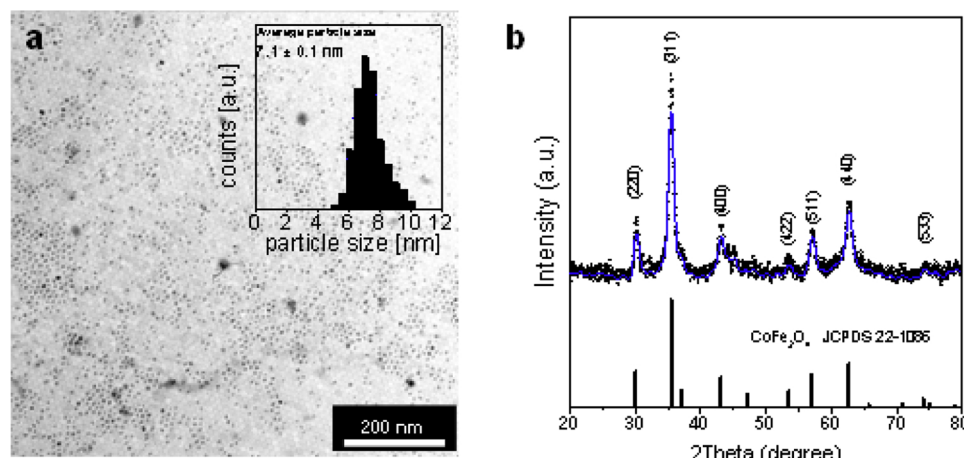


Fig. 1. a) Representative TEM micrograph of as-prepared CoFe₂O₄ NPs. Inset displays the corresponding size distribution histogram from where an average NP diameter of 7.1 ± 0.1 nm was estimated. b) XRD pattern of the as-prepared CoFe₂O₄ NPs. Graph includes the reference pattern JCPDS 22-1086 for the cubic CoFe₂O₄ crystal phase.

However, most of these studies have been limited to small-scale electrodes or have relied on costly and energy-intensive deposition methods. These studies consequently lack of the scalability feature, which is crucial for commercial application. Against this backdrop, the present study is dedicated toward the realization of a prototype electrolyser utilizing a potentially low-cost, scalable and high throughput process for the realization of high-performing and environmentally friendly OER catalysts on large-scale electrode scaffolds.

Among non-noble OER catalysts, some spinel-type binary transition metal oxides (AB₂O₄, A, B = metal) come to the fore owing to their high abundance, low toxicity, rich redox chemistry and chemical robustness [9–11]. Besides, bimetallic catalysts offer additional degrees of freedom compared to elemental compositions, enabling further optimization of active sites towards OER catalytic steps. Among these bimetallic oxide catalysts, Co-Fe spinel compounds are a particularly interesting case of a highly abundant and potentially low-cost material that shows excellent activity toward water oxidation [12–18].

While oxides offer high electrochemical stability, they usually suffer from intrinsically inferior electrical conductivities. To circumvent this issue and at the same time maximize the density of potential catalytic sites, oxide nano-domains need to be evenly distributed through the surface of a highly conductive scaffold that facilitates the charge transfer of the conjoint OER system. However, previous studies on CoFe₂O₄ particles loaded on high surface area scaffolds, such as doped carbon nanofibers [15] or hematite nanorods [19], were limited to laboratory-scale applications due to the complexity and high cost of the utilized synthesis routes and the difficulties that supporting such particles onto a large area three-dimensional (3D) scaffold involve [20].

Herein, we developed a potentially low-cost, scalable, high throughput and high yield method to produce CoFe₂O₄ ferrite nanoparticles (NPs). Additionally, we optimized the loading of the active NPs on large-scale Ni foams (NFs), as highly conductive, 3D and cost-effective electrode scaffold. Following the optimization of the loading process and the loaded amount of NPs, electrodes based on NFs coated with CoFe₂O₄ NPs were tested in a three-electrode set-up, as well as in a scaled-up two-electrode prototype electrolysis system to assess their viability for high yield H₂ production. We provide evidence that the used strategy bears great benefits regarding scalable preparation of high surface area and high activity catalysts. Additionally, we demonstrate the distribution and loading of oxide NPs to have a strong influence on the OER performance. Furthermore, we assessed the versatility of the presented system to be combined with renewable power sources by coupling the electrolyzer to a thin-film silicon solar cell for bias-free solar water splitting. Overall, the presented results set a new benchmark performance for transition metal oxides anchored on large-scale electrode support for the OER. These results will contribute to push the frontier of the field of environmentally friendly processes and

electrodes for commercially viable water electrolysis [21], electrochemical alcohol oxidation [22], waste water treatment [23], or nitrate reduction systems [24].

2. Experimental section

2.1. Chemicals and materials

Cobalt(II) acetylacetone (Co(acac)₂, 97%, Sigma-Aldrich), Iron acetylacetone (Fe(acac)₃, 97% Sigma-Aldrich), oleylamine (OAm, 80–90%, TCI), oleic acid (OAc, Sigma-Aldrich), Nafion (10 wt%, perfluorinated ion-exchange resin, dispersion in water), methanol (anhydrous, 99.8%, Sigma-Aldrich), carbon black (CB, VULCAN XC72), potassium hydroxide (KOH, 85%, Sigma-Aldrich), tetrafluoroboric acid (HBF₄, 48% Gew in H₂O Sigma-Aldrich) and acetonitrile (CH₃CN, extra dry, Fisher) were used as received without any further treatment. Chloroform, hexane, acetone, and ethanol were of analytical grade and purchased from various sources. Milli-Q water was obtained from a PURELAB flex from ELGA. An argon-filled glove box was used for storing and handling sensitive chemicals.

2.2. Synthesis of colloidal CoFe₂O₄ nanoparticles

All the syntheses were performed using standard airless techniques, i.e. a vacuum/dry argon gas Schlenk line. CoFe₂O₄ NPs were synthesized by loading 1.0 mmol of Fe(acac)₃, 1 mmol of Co(acac)₂, 10 ml OAm and 1.0 ml OAc in a three-neck flask and degassed under vacuum at 80 °C for 1 h while being strongly stirred using a magnetic bar. Subsequently, the reaction flask was heated to 230 °C and maintained for 30 min, while continuously adding nitrogen into the flask. A visible color change was observed immediately (see Scheme 1). The obtained NPs were collected by centrifuging and washing the solid product with acetone and hexane three times. The as-prepared NPs were finally dispersed in hexane with a concentration of 10 mg/mL and stored for further use. NPs were colloidally stable in chloroform for a couple of weeks.

2.3. Ligand removal

In a typical process, 10 mL of CoFe₂O₄ NPs dispersion in hexane (10 mg/mL) was combined with 10 mL acetonitrile to form a two-phase mixture and then a 1 mL HBF₄ solution (48%) was added. The resulting solution was sonicated until the NPs transferred from the upper to the bottom layer. The surface modified NPs were washed with ethanol for three times and dispersed in 10 mL ethanol with a small amount of DMF for further use.

2.4. Coating of Ni foam

2.4.1. Drop casting

Ni foam was sonicated in acetone, 1 M HCl, Milli-Q water, and ethanol respectively. 50 μ L of 10 mg/mL CoFe₂O₄ ethanol solution was dropped on nickel foam and dried in air and subsequently annealed at 400°C under nitrogen atmosphere.

2.4.2. Dip coating

Ni foam was sonicated in acetone, 1 M HCl, Milli-Q water, and ethanol respectively. In a typical process, clean and dry nickel foam was immersed in 10 mg/mL CoFe₂O₄ ethanol solution for 2 s and then taken out quickly and dried in air. This process was repeated for 1, 3, 5, and 7 times and denoted as 1 dip, 3 dips, 5 dips and 7 dips, respectively. The coated NFs were subsequently annealed at 400 °C under nitrogen atmosphere. After 3 dips the CoFe₂O₄ NP loading was 3.3 mg, about 1.15 mg/cm². (Fig. S5).

2.5. Characterization

Structural characterization was carried out by X-ray diffraction (XRD). The samples were scanned from 20 = 20° to 80° at a rate of 0.02 s⁻¹ in Bragg-Brentano geometry. The diffractometer was equipped with a Cu K α (1.54051 Å) radiation source. The morphology of the as deposited foam-based electrodes was observed using a scanning electron microscope (SEM) and elemental analysis was performed by the same microscope equipped with an X-ray energy dispersive spectrometer (EDS). The samples for transmission electron microscopy (TEM) were prepared by scratching the as-prepared CoFe₂O₄ powders from the Ni foam substrate, followed by dispersing them in hexane and collecting them on the TEM copper grids. High resolution transmission electron microscopy (HRTEM) images and scanning transmission electron microscopy (STEM) studies were conducted by using an FEI Tecnai F20 field emission gun microscope operated at 200 kV with a point-to-point resolution of 0.19 nm, which is equipped with high angle annular dark field (HAADF) and electron energy loss spectroscopy (EELS) detectors. X-ray photoelectron spectroscopy (XPS) was done on a SPECS system equipped with an Al anode XR50 source operating at 150 mW and a Phoibos 150 MCD-9 detector. The pressure in the analysis chamber was below 10⁻⁷ Pa. The area analyzed was about 2 mm × 2 mm. The pass energy of the hemispherical analyzer was set at 25 eV and the energy step was set at 0.1 eV. Data processing was performed with the CasaXPS program (Casa Software Ltd., UK). Binding energy values were centered using the C 1s peak at 284.8 eV. Fourier transform infrared (FTIR) spectra were recorded on an Alpha Bruker spectrometer.

The electrochemical performance of CoFe₂O₄@NF electrodes towards OER reduction was assessed using a three-electrode set-up. A leak-free Ag/AgCl 3.4 M KCl reference electrode (RE) was assembled in the polytetrafluoroethylene (PTFE) frame of the cell and placed very close to the working electrode surface. The potential was transformed to the reversible hydrogen electrode (RHE) scale: E (V_{RHE}) = E (V_{Ag/AgCl}) + 0.0592 × pH + 0.197. The data presented for the electrochemical characterization in aqueous solutions in three-electrode configuration do not include compensation for the series resistance of the solution. For the complete electrolyzer characterization, an adapted flow cell set-up (Micro Flow Cell, Electrocell A/S) was employed, schematically depicted in Fig. 7a. The flow rates of electrolytes within the flow cell were kept at 20 ml/min. As illustrated in Fig. 7a, the electrolyte was directly introduced through the macroporous 3D CoFe₂O₄@NF electrode (geometric surface area: 10 cm²). For details on the cyclic voltammetry (CV) and gas chromatography (GC) regarding the assessment of current-voltage behavior and the faradaic efficiency for gaseous products, respectively, the reader is referred to Ref. [41] and Ref. [42]. The electrically attached triple junction thin-film silicon device had an area of 1 cm², thus during the photoelectrolysis measurement an area of 1 cm² was illuminated. All photoelectrochemical

experiments were conducted using a solar simulator equipped with a 150 W xenon lamp. The intensity of the light source was adjusted to match standard AM 1.5 G sunlight at 100 mW/cm² intensity. The experiments for the full system assembly were carried out in a two-electrode configuration. The faradaic efficiency to H₂ was calculated using the analysis of the outlet gas by gas chromatography (GC) during potentiostatic measurements. Helium (99.999%) was used as the carrier gas. The calibration of peak area vs. gas concentration was used for the molar quantification of each gaseous effluent. The faradaic efficiency was calculated by determining the number of coulombs needed for each product and then dividing by the total charge passed during the time of the GC sampling according to the flow rate. In the photovoltaic-electrolyzer coupled system, to account for deviations in the assessment of the photovoltaic performance of the complete system, i.e. spectra variations due to diode calibration accuracy, area definition, or temperature variation, a systematic error of 2% was considered [25].

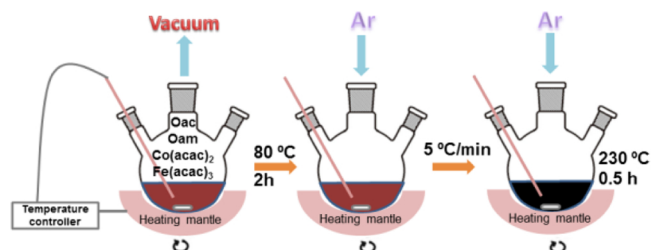
3. Results

3.1. Synthesis and characterization of colloidal CoFe₂O₄ NPs

Co-Fe oxide NPs were produced in colloidal form from the reduction of cobalt and iron salts in the presence of OAm and OAc and the posterior oxidation of the reaction product in ambient conditions (Scheme 1, see Experimental Section for details). A representative TEM micrograph and the size distribution histogram of the oxidized NPs are shown in Fig. 1a. Co-Fe oxide NPs displayed a quasi-spherical geometry, with an average diameter of 7.1 ± 0.1 nm. In contrast to the product of the oxidation of iron NPs, the oxidation of Co-Fe NPs did not result in the formation of hollow structures, probably due to the relatively low diffusivity of Fe and Co through the growing Co-Fe oxide shell compared with that of Fe though FeO/γ-Fe₂O₃ [26–28].

XRD analysis revealed Co-Fe oxide NPs to crystallize in the CoFe₂O₄ cubic phase (JCPDS 22-1086, Fig. 1b). HRTEM micrographs confirmed the crystal structure of the NPs to be compatible with the CoFe₂O₄ ferrite cubic phase ([FM3-MZ]-Space group 227) with lattice parameters $a = b = c = 0.83961$ nm (Fig. 2b). HAADF-STEM and EELS analysis demonstrated the three constituent elements, Co, Fe, and O, to be present in the same ratio in all NPs and to be homogeneously distributed within each NP (Fig. 2a).

N₂ adsorption–desorption isotherms of the CoFe₂O₄ NPs dried in the form of a powder displayed a type-I reversible behavior (Fig. 3), which is generally a signature of microporous solids [29]. CoFe₂O₄ nanopowders were characterized by a Langmuir specific surface area (SSA) of 276 m²/g and a Brunauer–Emmett–Teller (BET) SSA of 174 m²/g. The obtained BET SSA is among the highest reported for Co-Fe spinel NPs, slightly above that of NPs synthesized by hydrothermal [13] and micro emulsion techniques [20] (~150 m²/g), and significantly higher than materials prepared by electrospinning [15] and electrodeposition [16] (~55 m²/g). Notice that these high SSAs were measured from the nanopowders obtained by drying the colloidal NPs in ambient conditions and with no pre-coordination of the NP into a network. Even larger SSA values would be potentially obtained through the formation



Scheme 1. Schematic illustration of the synthesis procedure used to prepare colloidal CoFe₂O₄ NPs.

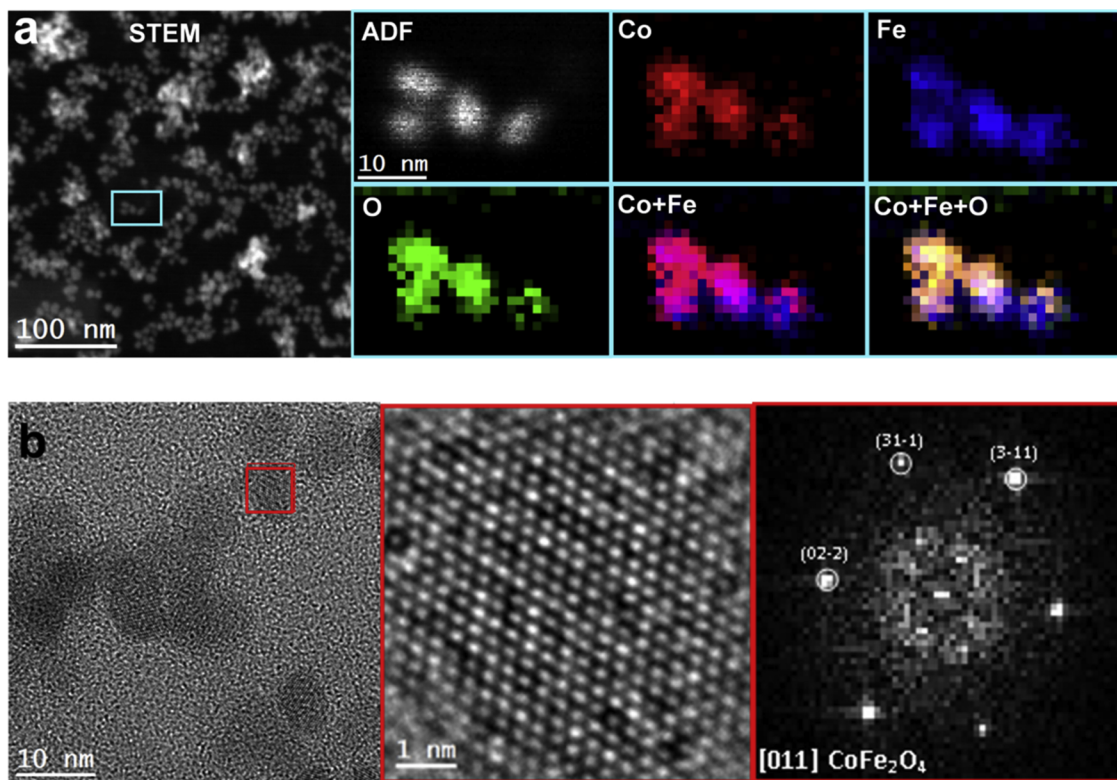


Fig. 2. a) HAADF-STEM micrograph and EELS chemical composition maps (from cyan rectangle) for Co (red), Fe (blue), O (green) and their composites. b) HRTEM micrograph, detail of the red squared region (scale bar, 1 nm), and corresponding FFT spectrum indicating that NPs crystallized in the cubic CoFe₂O₄ phase, [FM3-MZ]-Space group 227, with lattice parameters of $a = b = c = 0.83961$ nm, and $\alpha = \beta = \gamma = 90^\circ$. (For interpretation of the references to colour in this figure legend, the reader is referred to the web version of this article).

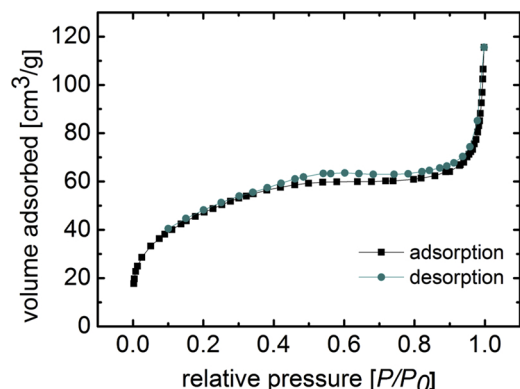


Fig. 3. N₂ adsorption–desorption isotherms from the CoFe₂O₄ nanopowders obtained from drying CoFe₂O₄ NPs under ambient conditions.

of NP networks in solution, i.e. NP gelation, and the posterior drying from supercritical CO₂ for instance [30,31].

3.2. Loading on large-scale Ni foams

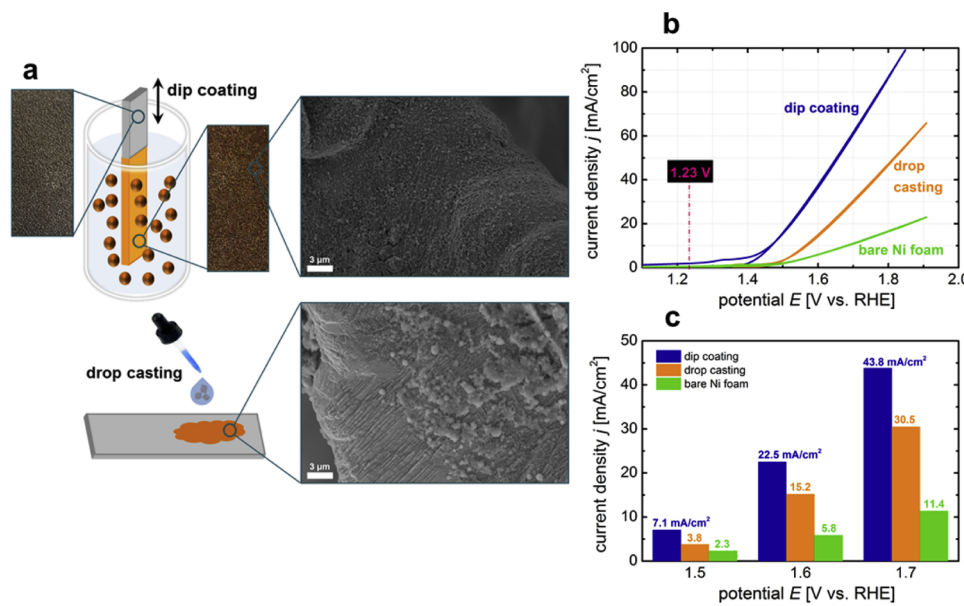
The optimized loading of nano-sized OER catalysts onto large-scale scaffolds is an important step toward the realization of industry-viable electrodes and electrolyzers. In this direction, we first studied the deposition of NPs on small (1 cm^2) NF electrodes and subsequently optimized the deposition process for larger scaffolds ($\geq 10\text{ cm}^2$). Before deposition, organic ligands at the surface of as-synthesized NPs, which were used to adjust NP growth during the synthesis, were removed using a solution of tetrafluoroboric acid in acetonitrile (see Experimental Section). After successive cleaning with tetrafluoroboric acid, FTIR spectra showed the disappearance of the peaks at 2822 and

2890 cm⁻¹ corresponding to CH– stretching modes, what evidenced the effective removal of hydrocarbon ligands (Fig. S3). This ligand displacement step is key towards producing high performance and reliable electrocatalysts since generally organic ligands strongly limit electronic transport and the ability of the NPs to interact with their surrounding media, i.e. with the scaffold and the electrolyte [32]. Furthermore, in the present case, the presence of organic ligands on the surface of the CoFe₂O₄ NPs impeded a homogeneous coating of the NF. Not mediating a ligand removal pretreatment, a porous two-dimensional organic film was deposited on the NF after dip coating it into a suspension of colloidal NPs (Fig. S2).

Two procedures were explored to support CoFe₂O₄ NPs on NFs: dip coating and drop casting. As depicted in Fig. 4a, the foam was either dipped into the dispersion of colloidal NPs and hold for 2 s or the suspension was dropped onto the foam (2 mg of solution) and let it dry. SEM characterization showed the dip coating process to result in a homogeneous distribution of NPs on the NF surface. On the other hand, drop-casted NFs displayed numerous NP agglomerates.

XPS survey spectrum of the CoFe₂O₄ NPs supported on the NF (3 dips) demonstrated the presence of Co, Fe, O, and Ni (Fig. S6). The Co 2p and Fe 2p spectra matched well with Co²⁺ and Fe³⁺ [33,34] and the O 1s spectrum displayed two peaks at about 531.1 and 532.4 eV which corresponded to oxygen in the metal–oxygen bond and hydroxyl groups, respectively [35]. Quantitatively, XPS analysis showed the atomic concentration of Fe on the surface to be a threefold of that of Co: Fe/Co = 3 (Table S1). Additionally XPS analysis showed a large surface Ni concentration, ca. 50 at% of the surface composition (Table S1). XRD and HRTEM analysis of the NPs after the annealing step, showed the CoFe₂O₄ crystal structure to be maintained (Figs. S8 and S9). SEM-EDX analysis showed a homogeneous distribution of the different elements on the NF (Fig. S10).

The electrochemical performance toward OER of NFs loaded with



CoFe_2O_4 NPs (hereafter $\text{CoFe}_2\text{O}_4@\text{NF}$) is shown in Fig. 4b. In comparison with bare NF, used in industrial water splitting, $\text{CoFe}_2\text{O}_4@\text{NF}$ electrodes displayed significantly enhanced OER catalytic activities. $\text{CoFe}_2\text{O}_4@\text{NF}$ electrodes provided much higher current densities under the same applied potential than bare NF (Fig. 4c). In addition, $\text{CoFe}_2\text{O}_4@\text{NF}$ electrodes prepared by dip coating provided higher performance over electrodes prepared by drop casting. This result was consistent with the usual assumption that thinly dispersed oxide nanoparticles favor electrochemical performance. A significant increase in the current density for potentials > 1.5 V was measured for samples prepared by dip coating, attaining $43.8 \text{ mA}/\text{cm}^2$ at $1.7 \text{ V}_{\text{RHE}}$ (470 mV overpotential), which is 1.4 times higher than the current density obtained with the drop casted sample (Fig. 4b).

The dip coating technique was further optimized for large area electrodes (10 cm^2). Fig. 5 presents SEM images of the NF surfaces after 1, 3, 5, and 7 dips (each hold for 2 s) into the CoFe_2O_4 NP suspension. After 1 dip, major parts of the NF remained uncovered, whereas 3 dips resulted in a high coverage of the NF surface with highly dispersed NPs

(Fig. S4). Increasing the number of dips to 5 led to the formation of NP aggregates with sizes ranging from 50 to 200 nm (Fig. 5). This effect was even more pronounced after 7 dipping times, resulting in an almost complete coverage of the NF surface by CoFe_2O_4 NP agglomerates.

The electrochemical characteristics of the large-scale $\text{CoFe}_2\text{O}_4@\text{NF}$ electrodes were assessed in a three-electrode configuration using 1 M KOH electrolyte solution (see Experimental Section). Fig. 6a shows the CV curves of the electrode samples investigated in Fig. 5. The number of dip coating steps had a significant influence on the OER performance. Best performances were achieved with $\text{CoFe}_2\text{O}_4@\text{NF}$ electrodes produced using 3 dip coating steps, in good agreement with the observed homogeneous coverage of the NF surface with thinly dispersed NPs. OER overpotentials of the four tested samples for different current densities are shown in Fig. 6b. $\text{CoFe}_2\text{O}_4@\text{NF}$ electrodes produced after 3 coating steps exhibited the lowest overpotentials, with 250 mV and 460 mV for $10 \text{ mA}/\text{cm}^2$ and $50 \text{ mA}/\text{cm}^2$, respectively. Higher CoFe_2O_4 NP loads containing NP agglomeration provided lower OER performance. This result is understandable as oxide structures generally suffer

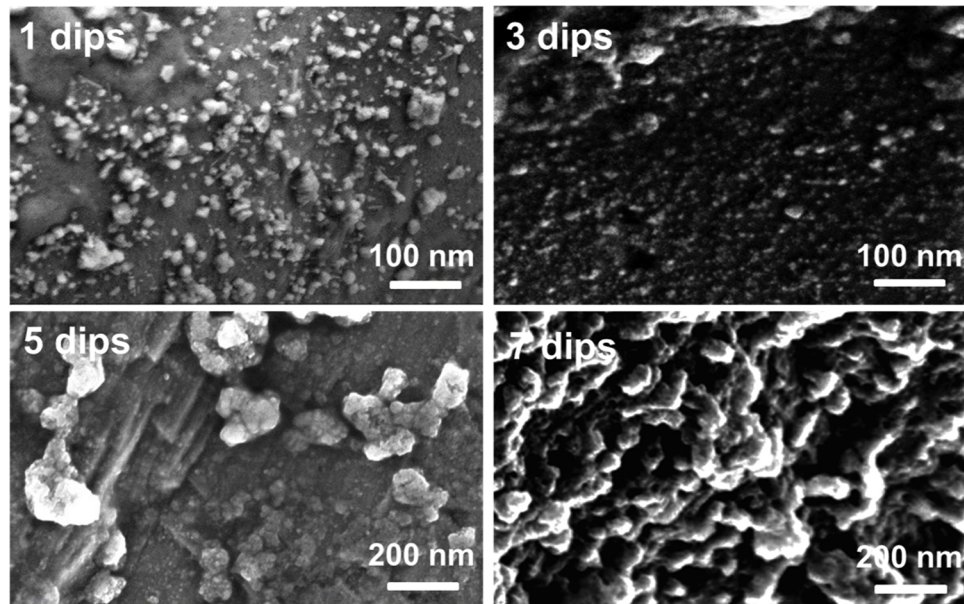


Fig. 5. SEM micrographs of $\text{CoFe}_2\text{O}_4@\text{NF}$ electrodes (10 cm^2) produced using different dip coating steps: 1, 3, 5, and 7 as noted in each micrograph.

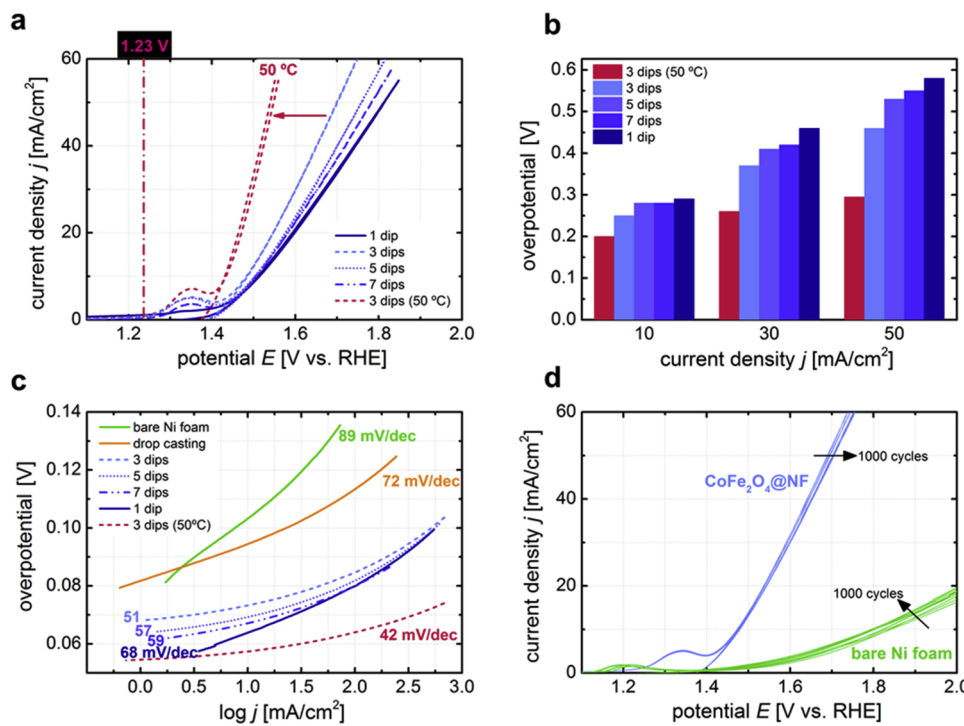


Fig. 6. a) CV curves of NF electrodes dipped into the CoFe_2O_4 NP solution, for 1 (solid), 3 (dashed), 5 (dotted), and 7 (dash-dotted) times. CV curves were measured in 1 M KOH at a scan rate of 10 mV/s. $\text{CoFe}_2\text{O}_4@\text{NF}$ electrodes providing best OER catalytic performances (3 dips) were measured under elevated electrolyte temperature (50 °C, pink dashed line). The $\text{H}_2\text{O}/\text{O}_2$ oxidation potential is indicated by the straight dash-dotted line. b) Required overpotentials derived from CV curves at different current densities. c) Tafel plots of the tested samples. d) CV curves of the $\text{CoFe}_2\text{O}_4@\text{NF}$ (3 dips) and bare NF electrodes, respectively, before and after 1000 cycles. Every 200th CV scan of each electrode is plotted.

from low electrical conductivities, which strongly limits the thickness of the oxide layer that can be practically used. The highest overpotential of 580 mV at 50 mA/cm² was measured for the 1 step coating $\text{CoFe}_2\text{O}_4@\text{NF}$ electrode, presumably due to an insufficient coverage of the scaffold with CoFe_2O_4 NPs (Fig. 5).

Commercial alkaline electrolyzers work at operating temperature between 25 and 100 °C, which is why we tested the best performing electrode (3 dips) also under elevated electrolyte temperature. As observed in Fig. 6a and b, the OER performance was significantly enhanced by increasing the electrolyte temperature up to 50 °C. Extremely low overpotentials of 200 mV and 295 mV for 10 mA/cm² and 50 mA/cm², respectively, were obtained. Fig. S12 show results obtained for 4 additional samples in the same conditions, demonstrating the reproducibility of our procedure. Temperature has a strong influence on the thermodynamic and kinetic functions, including electronic, ionic and molecular diffusion. Increasing temperature can accelerate the reaction kinetics, improve diffusion, disturb the electrochemical double layer and increase the electrical conductivity of the electrolyte solution, among other, all of them having an important and beneficial influence on the OER performance [36–38].

We further compared the performance of the $\text{CoFe}_2\text{O}_4@\text{NF}$ electrodes with that of other electrodes prepared from supporting the CoFe_2O_4 on other substrates, including Cu foam and carbon cloth (Fig. S13). The incorporation of the CoFe_2O_4 NPs on any of the substrates significantly reduced their overpotential. Among the different substrates, $\text{CoFe}_2\text{O}_4@\text{NF}$ electrodes achieved the best performance, with an overpotential down to 250 mV at 10 mA/cm². Such value is below that of most of state-of-the-art OER electrodes in literature, evidencing the high potential for commercial applications of the herein developed large-scale $\text{CoFe}_2\text{O}_4@\text{NF}$ OER electrodes. State-of-the-art electrocatalytic properties toward OER of previously reported Co-Fe and NF-based electrodes are summarized in Table S2 in the SI.

The electrocatalytic kinetics for OER of the $\text{CoFe}_2\text{O}_4@\text{NF}$ electrodes were further investigated by Tafel plots (Fig. 6c). For comparison, the Tafel plots of the sample prepared by drop casting and the bare NF sample are also shown in Fig. 6c. In accordance with the results shown in Fig. 4b and c, the drop casted and the bare NF electrodes exhibited the worst kinetics among the analyzed electrodes, i.e. the highest Tafel

slopes, at 89 mV/dec and 72 mV/dec, respectively. For the $\text{CoFe}_2\text{O}_4@\text{NF}$ electrodes prepared by dip coating, Tafel slopes were impressively low and ranged from 68 mV/dec for the 1 time dipped sample to 51 mV/dec for the 3 times dipped electrode. Hence, our $\text{CoFe}_2\text{O}_4@\text{NF}$ electrodes showed comparable and even better electrocatalytic properties toward OER than related nonprecious metal-based OER electrocatalysts reported in literature (Table S1 of the SI). The $\text{CoFe}_2\text{O}_4@\text{NF}$ electrode measured in a 50 °C alkaline solution provided the lowest Tafel slope, 42 mV/dec, as could be expected from the corresponding CV curve in Fig. 6a. In fact, such an outstanding kinetic behavior made it an ideal anode candidate for commercial electrolysis systems.

XPS analysis of the electrodes after long term cycling showed no significant difference in the chemical environment of Co and Fe with respect to the results obtained from electrodes after annealing (Fig. S7). However, quantitatively, after long term cycling the amount of Fe detected on the electrode surface was significantly lower from the initial $\text{Fe}/\text{Co} = 3$ to the final $\text{Fe}/\text{Co} = 0.5$ (Table S1). In parallel, the concentration of Ni significantly increased, from 50 at% to up to an 80 at% (Table S1). On the other hand, SEM-EDX analysis showed a similar Co and Fe concentration on top of the NF. We hypothesize that during cycling a significant amount of Ni from the NF is able to diffuse within the CoFe_2O_4 structure and to accumulate, together with Co, on the NP surface, partially displacing Fe ions. The presence of these Ni ions on the catalyst surface may contribute to the outstanding performance obtained from $\text{CoFe}_2\text{O}_4@\text{NF}$ electrodes compared with other supports and literature results (Fig. S13 and Table S2).

Besides electrochemical performance, durability is another major parameter in the realization of industry-viable electrodes for electrolyzers. In this direction, we investigated the long-term stability for $\text{CoFe}_2\text{O}_4@\text{NF}$ electrodes (3 dips) by cycling them 1000 times in 1 M KOH at ambient temperature (Fig. 6d). Again, bare NF was utilized for comparison. $\text{CoFe}_2\text{O}_4@\text{NF}$ electrodes showed a negligible degradation after continuous 1000 CV cycles, indicating its superior operational stability under alkaline test condition. XPS and XRD analysis of the material after long term cycling (Figs. S7 and S8) also showed the chemical environment of Co and Fe and the crystal structure of the NPs to remain unmodified. The mechanical and structural stability was further confirmed by HRTEM analysis of the used catalyst, showing the

CoFe_2O_4 NPs to remain thinly dispersed onto the NF and maintaining their size after the long-term experiment (Fig. S9). No obvious NP aggregation/growth was observed, which was associated to the proper immobilization of the CoFe_2O_4 NP on the NF. Consistently with previous reports, bare NF slightly increased its activity towards OER with time (Fig. 6d). In alkaline solution, this activity enhancement has been associated to the contribution to the catalytic activity of metallic impurities (e.g. Fe) from the electrolyte that are deposited onto the Ni surface during long-term operation [40]. Because such a behavior was not observed with CoFe_2O_4 @NF electrodes, we assume that the Ni scaffold have a moderate catalytic role in this system.

We estimated the electrochemical active surface area (ECSA) of CoFe_2O_4 @NF (3 dips) and bare NF electrodes from the electrochemical double-layer capacitance (Cdl) at the solid/liquid interface [41]. Figs. S14a and S14b (SI) present the CV curves of the two electrodes recorded in a non-Faradic potential range under different scan rates. CoFe_2O_4 @NF cathodes exhibited a higher Cdl than bare NF, evidencing a higher active surface area, which was estimated as 80.5 cm^2 for CoFe_2O_4 @NF and 31.0 cm^2 for bare NF (Fig. 6c). This result probes the CoFe_2O_4 @NF to provide a larger number of catalytically active sites and thus an improved OER activity, much higher than that of CoFe_2O_4 NPs on carbon nanofibers (20.6 cm^2) and commercial RuO_2 catalyst (14.5 cm^2) [15].

3.3. Prototype electrolysis reactor

The optimized large-scale CoFe_2O_4 @NF electrode was subsequently integrated in a prototype electrolysis reactor [41–44]. As illustrated in Fig. 7a, the reactor design allowed to work under flow conditions, where the anolyte and catholyte solutions are continuously recirculated through the respective compartments, i.e. a CoFe_2O_4 @NF anode compartment performing the OER and a Ti/Pt cathode compartment performing the hydrogen evolution reaction (HER). By this design, the flow dynamics of the electrolysis set-up could be significantly enhanced, fostering higher electrochemical activity. Both compartments were separated by a membrane and a gas chromatograph was employed for gaseous product identification. The configuration can even be adapted

for the additional integration of photovoltaic devices, as shown in Fig. 7a with a thin-film silicon solar cell (see Experimental Section for details).

The characteristics of the complete reactor in two-electrode operation are shown in Fig. 7b for two different configurations. The first configuration consisted in using a cation-exchange membrane (Nafion®117) and 1 M KOH electrolyte solution in both compartments. In the second configuration, we applied a bipolar membrane (BPM), enabling to operate the electrolysis reactor with two different electrolytes. In this configuration, we applied a 1 M KOH (pH = 13.7) for the anolyte to perform the OER and a 1 M H_2SO_4 (pH = 0) solution for the catholyte to perform the HER. As can be seen from the linear sweep voltammetry (LSV) curves in Fig. 7b, the configuration using the BPM exhibited a better overall electrolysis behavior than the reactor configuration containing the Nafion membrane. To provide 200 mA and 400 mA, respectively, the BPM configuration only required 1.51 V and 1.59 V, respectively, whereas in the Nafion configuration the complete electrolyser cell voltage augmented to 1.60 V and 1.76 V, respectively. The higher cell voltage was related with the reduced electrochemical performance of the Ti/Pt cathode in alkaline solution (Nafion configuration) compared to its performance in acid electrolytes (BPM configuration). In Fig. S15, the LSV curves of Ti/Pt in 1 M KOH and 1 M H_2SO_4 electrolyte solution are shown. LSV curves displayed overpotentials of 340 mV and 180 mV at 50 mA/cm² for basic and acidic catholytes, respectively, further demonstrating the superior cathode performance in acidic medium. To simulate real electrolyser conditions, the overall polarization of the reactor device was also measured at elevated electrolyte temperatures (50 °C) in the BPM configuration. As expected from the results shown in Figs. 6a and S15, the electrochemical performance increased with increasing electrolyte temperature, reaching complete electrolyzer cell voltages of 1.46 V and 1.51 V to produce 200 mA and 400 mA, respectively. From these values, electrochemical energy efficiency up to 75% and 81%, for ambient and elevated operation temperatures were calculated. Consequently, the herein proposed electrolyzer based on a CoFe_2O_4 @NF electrode presents an attractive alternative to commercial systems used for surplus electric power storage, such as pumped hydroelectric storage (70–80%

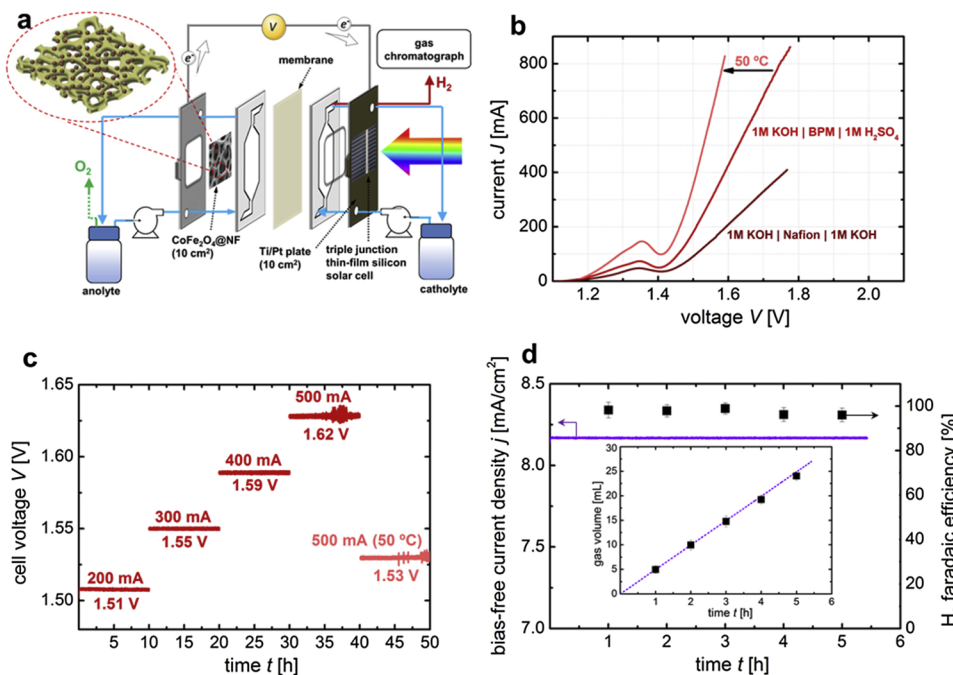


Fig. 7. a) Sketch of the experimental prototype reactor used to assess the overall electrolysis performance. The illustration shows the different components, including a schematic illustration of the 3D NF coated with CoFe_2O_4 NPs and the coupled triple junction thin-film silicon solar cell (a-Si:H/a-Si:H/μc-Si:H) for the bias-free operation test (see Fig. 7d). b) Linear sweep measurements of the CoFe_2O_4 @NF electrodes (10 cm^2 geometric area) combined with the Ti/Pt cathode (10 cm^2 geometric area) for a configuration containing Nafion and BPM membrane, respectively. The BPM configuration (best performing) was also measured at 50 °C electrolyte solution (1 M KOH). c) Long-term behavior of the electrolysis showing the required cell voltages of the reactor as a function of the applied current (each galvanostatic testing was conducted for ~10 h with the same electrodes and membrane). d) Bias-free solar water splitting using a triple junction a-Si:H/a-Si:H/μc-Si:H solar cell (as depicted in a)). Left y-axis shows the achieved bias-free current density over the operation time. Right y-axis represents the faradaic efficiency for H_2 production over the operation time. The error bars indicate standard deviations obtained from 3

experimental repeats. The inset shows the calculated gas volume obtained. The dotted purple line shows the theoretical (assuming 100% faradaic efficiency) gas evolution for the measured bias-free current density and the black squares show the experimental values. (For interpretation of the references to colour in this figure legend, the reader is referred to the web version of this article).

efficiency), power-to-gas based on alkaline and PEM electrolyzers (65–70% efficiency), or ion lithium batteries (92–95% efficiency) that have other severe limitation in terms of energy density, cost and life time.

The electrochemical durability of the prototype reactor was assessed by conducting chronoamperometry. Fig. 7c displays the electrolyzer cell voltages at successively increasing electrolysis currents of 200, 300, 400, and 500 mA applied for 10 h each, until a total of 50 h of continuous operation. The prototype electrolyzer showed no sign of decay when operated for 50 h, even when operated at higher temperature (50 °C).

Given its remarkable activity and high electrochemical energy efficiency, the prototype electrolysis reactor can be effectively powered by renewable energy sources, such as photovoltaics [25,42]. In this direction, the conversion of solar energy into chemical fuels energy is a promising route for future conversion and storage concepts. Solar-to-fuel conversion efficiencies using photovoltaics and electrolyzers depends on the efficiency of the two systems. Taking into account electrochemical conversion efficiency above 80% as reached for CoFe_2O_4 @NF electrodes, their combination with commercial high efficiency solar cells having 30% conversion efficiencies could result in 24% solar-to-fuel conversion efficiencies. However, in the present work, to achieve cost-effectiveness, we aimed at reducing the system cost using amorphous silicon solar cells. Thus, we electrically connected the prototype electrolyzer to a low-cost triple junction a-Si:H/a-Si:H/μc-Si:H solar cell with a photovoltaic conversion efficiency of around 13.4% (Fig. 7a.) [25]. In figure S16, the system current density-voltage (j - V) curve is overlaid with the polarization curve of the electrolyzer device. The crossing point of both j - V curves, which can serve to estimate the bias-free operation current density of the solar-driven electrolyzer, lied in the plateau region of the solar cell characteristics (near the maximum power point) at 1.45 V and 8.2 mA/cm^2 . The bias-free measurement of the solar-driven electrolyzer is shown in Fig. 7d. This result demonstrates that the prototype electrolyzer can be powered only by sunlight energy, providing current densities up to $8.2 \pm 0.2 \text{ mA/cm}^2$. The faradaic efficiency for H_2 production, measured by gas chromatography, was found to be close to 100% over the course of bias-free operation ($> 5 \text{ h}$), as depicted on the right ordinate in Fig. 7d. The inset in Fig. 7d shows the theoretical and experimentally determined bias-free H_2 gas production over time, proving that H_2 was the only product formed during electrolysis (besides O_2). With these values, a solar-to-hydrogen conversion efficiency of $10.0 \pm 0.2\%$ was calculated, which is among the record bias-free water splitting efficiencies for thin-film silicon based devices [25,45,46]. Overall, this example demonstrates that electrolyzers based on CoFe_2O_4 @NF electrodes can match the stringent requirements for cost-effective renewable energy conversion and storage at large scale.

4. Discussion

The enhanced OER catalytic activity of the CoFe_2O_4 @NF electrodes here presented can be ascribed to the combination of nano-sized active CoFe_2O_4 particles with the 3D macroporous structure of the supporting NF, as illustrated in Fig. 7a. This marriage resulted in a significantly increased contact area between catalysts and electrolytes and provided a greater amount of active sites where OER could take place (see ECSA estimation in the SI, Figures S14c). The dip coating procedure eventually led to an optimum distribution of thinly dispersed CoFe_2O_4 NPs (Fig. 5), which allowed to circumvent the intrinsically inferior electrical conductivity of oxide particles (see low Tafel slopes in Fig. 6c), while ensuring an impressive stability of the CoFe_2O_4 @NF electrode (Figs. 6d and 7c).

The large-scale electrode used, the high stability demonstrated and the low electrolyzer cell voltages at industrial relevant currents and at ambient and elevated temperature probed the technology relevance of the present system. Values reported here are among the record

performance indices for overall water splitting using inexpensive and earth-abundant catalysts. Additionally, the present study assessed their performance on large-scale electrodes in a prototype electrolyzer. While the aspect of process scalability is vital in view of a real-world application, it has neither been experimentally evidenced, nor sufficiently discussed in previous related studies on OER materials (exemplarily see electrode areas in Table S1 in the SI). These previous studies focused on laboratory scale electrodes, neglecting critical issues, which have been addressed in the present study, such as homogeneous coverage of active electrocatalyst on large-scale scaffolds, higher chemical resistivity or low-cost and high throughput and yield processing techniques.

In general, the coupling of pure academic with engineered systems is urgently needed to mature renewable fuel production processes and open the pathway towards commercial application. This aspect is successfully addressed by the herein proposed system. In addition, the scalable process of the developed CoFe_2O_4 @NF electrode paired with the adaptability of the presented prototype reactor bears great benefits and cross-fertilization for a number of related catalytic and photovoltaic technologies. Thus, our electrolyzer concept is not limited to small active electrode areas [47,48] or expensive small-scale photovoltaic structures [49] but can be adapted to large scale designs. Nevertheless, from a scientific point of view, further attention should be devoted to investigate earth-abundant and active HER electrodes. The herein applied Ti/Pt plate served as stable and reliable proof-of-concept electrode, but could be replaced by a cathode system, which does not contain rare materials such as Pt. From a more engineering point of view, the evaluation of different approaches to upscale the photovoltaic structures up to the geometric size of the electrochemical active surface areas could be alluring if integrated photoelectrochemical cell (PEC) systems are envisaged. In this “PEC-farm” approach, multiple medium-scaled electrolyzers, i.e. electrolyzers similar to the herein presented prototype (10–100 cm^2 active photovoltaic and electrochemical electrode areas), could operate independently, while the produced fuels of all the electrolyzers would be collected together [50]. The advantageous feature of this concept is that lower photocurrent densities would be required, which would be beneficial regarding lower overpotential losses and thus, eventually higher overall solar-to-fuel efficiencies. In this regard, it is projected by techno-economic models of large scale, centralized solar H_2 production facilities that overpotential losses at high operating current densities are one of the most important factors in reducing the STH efficiency and thus, increasing the cost of H_2 [51,52].

In total, all these examples manifest the high versatility and cross-fertilization of the herein presented scalable CoFe_2O_4 @NF electrode and electrolysis system, respectively.

5. Conclusion

In conclusion, we have presented a simple and scalable colloidal synthesis and coating strategy for the homogeneous anchoring of bi-metallic CoFe_2O_4 NPs on large-scale NF. CoFe_2O_4 @NF electrodes were demonstrated to be an efficient earth-abundant OER electrocatalysts with ultralow overpotential, large current density, small Tafel slope, and long-term durability in alkaline solution. The improved catalytic performances are believed to originate from the unique synergy between the nano-scaled active CoFe_2O_4 NPs and the highly conductive and high area Ni scaffold. The interdiffusion of Ni ions from the Ni scaffold to the CoFe_2O_4 NPs may also contribute to improve catalytic performance. Considering cost-effectiveness, facile, as well as reliable fabrication processes, and the outstanding catalytic performance of CoFe_2O_4 @NFs may hold great potential in future energy conversion and storage devices. Moreover, the performance of the large-scale CoFe_2O_4 @NF (10 cm^2 geometric active area) was investigated in a prototype electrolysis reactor, where currents of 500 mA were achieved with electrolyzer cell voltages of 1.62 V and 1.53 V at ambient and elevated temperatures, respectively, over prolonged operation times. Overall, the presented electrochemical results paired with the versatile

synthetic and coating strategy may stimulate future lines of work, which will be needed to address efficiency improvements and technological questions while assessing cost competitiveness of promising (photo)-electrochemical technologies.

Author contributions

F.U., J. R. M. and A.C. conceived the project and designed the experiments. F.U. carried out the (photo)-electrochemical experiments. R.D. conducted the synthesis and coating of the Ni foam. P.Y.T., R.D. and J.A. conducted the structural and compositional analyses. F.U., R.D. and P.Y.T. interpreted data. F.U. wrote the manuscript. V.S. and F.F. performed and supervised the deposition of the multijunction thin-film silicon solar cells. J.R.M. T.A. and A.C. supervised the proposed and executed research program. All the authors participated in discussions and contributed to editing of the manuscript.

Declaration of Competing Interest

The authors declare no conflict of interest.

Acknowledgments

Authors acknowledge funding from Generalitat de Catalunya through the CERCA program, 2017 SGR 1246, 2017 SGR 327 and the Spanish MINECO projects MAT2014-59961, ENE2016-80788-C5-5-R, ENE2016-77798-C4-3-R and ENE2017-85087, together with the support from Repsol S. A. Likewise, the authors thank Enagás S.A. ICN2 is supported by the Severo Ochoa program from Spanish MINECO (Grant No. SEV-2017-0706). IREC also acknowledges additional support from the European Regional Development Funds (ERDF, FEDER), (S)TEM part of the present work has been performed in the framework of Universitat Autònoma de Barcelona Materials Science PhD program and the rest in the Nanoscience program of the University of Barcelona. The authors thank S. Moll (IEK-5), M. Biset-Peiró (IREC), and H. Xie (IREC) for their contribution to this work. F.U. acknowledges financial support from MINECO through Juan de la Cierva fellowship (FJCI-2016-29147). V.S. and F.F. (authors from IEK-5) thank the Deutsche Forschungsgemeinschaft (DFG) (Priority Program SPP 1613). J. Llorca is a Serra Húnter Fellow and is grateful to ICREA Academia program and funding from Generalitat de Catalunya 2017 SGR 128.

Appendix A. Supplementary data

Supplementary material related to this article can be found, in the online version, at doi:<https://doi.org/10.1016/j.apcatb.2019.118055>.

References

- [1] S.B. Walker, U. Mukherjee, M. Fowler, A. Elkamel, Benchmarking and selection of Power-to-Gas utilizing electrolytic hydrogen as an energy storage alternative, *Int. J. Hydrogen Energy* 41 (2016) 7717–7731, <https://doi.org/10.1016/j.ijhydene.2015.09.008>.
- [2] N.-T. Suen, S.-F. Hung, Q. Quan, N. Zhang, Y.-J. Xu, H.M. Chen, Electrocatalysis for the oxygen evolution reaction: recent development and future perspectives, *Chem. Soc. Rev.* 46 (2017) 337–365, <https://doi.org/10.1039/C6CS00328A>.
- [3] C.C.L. McCrory, S. Jung, I.M. Ferrer, S.M. Chatman, J.C. Peters, T.F. Jaramillo, Benchmarking hydrogen evolving reaction and oxygen evolving reaction electrocatalysts for solar water splitting devices, *J. Am. Chem. Soc.* 137 (2015) 4347–4357, <https://doi.org/10.1021/ja510442p>.
- [4] S. Ardo, D.F. Rivas, M.A. Modestino, V.S. Greiving, F.F. Abdi, E.A. Llado, V. Artero, K. Ayers, C. Battaglia, J.-P. Becker, Pathways to electrochemical solar-hydrogen technologies, *Energy Environ. Sci.* 11 (2018) 2768–2783, <https://doi.org/10.1039/C7EE03639F>.
- [5] M. Ball, M. Weeda, The hydrogen economy—vision or reality? *Int. J. Hydrogen Energy* 40 (2015) 7903–7919, <https://doi.org/10.1016/j.ijhydene.2015.04.032>.
- [6] T. Rostrup-Nielsen, Manufacture of hydrogen, *Catal. Today* 106 (2005) 293–296, <https://doi.org/10.1016/j.cattod.2005.07.149>.
- [7] K. Chakrapani, G. Bendt, H. Hajiyani, I. Schwarzkroch, T. Lunkenbein, S. Salamon, J. Landers, H. Wende, R. Schlögl, R. Pentcheva, Role of composition and size of cobalt ferrite nanocrystals in the oxygen evolution reaction, *ChemCatChem.* 9 (2017) 2988–2995, <https://doi.org/10.1002/cctc.201700376>.
- [8] H. Zhou, F. Yu, Q. Zhu, J. Sun, F. Qin, L. Yu, J. Bao, Y. Yu, S. Chen, Z. Ren, Water splitting by electrolysis at high current densities under 1.6 volts, *Energy Environ. Sci.* 11 (2018) 2858–2864, <https://doi.org/10.1039/C8EE00927A>.
- [9] T. Maiyalagan, K.A. Jarvis, S. Therese, P.J. Ferreira, A. Manthiram, Spinel-type lithium cobalt oxide as a bifunctional electrocatalyst for the oxygen evolution and oxygen reduction reactions, *Nat. Commun.* 5 (2014) (2014) 3949, <https://doi.org/10.1038/ncomms4949>.
- [10] M. Tahir, L. Pan, F. Idrees, X. Zhang, L. Wang, J.-J. Zou, Z.L. Wang, Electrocatalytic oxygen evolution reaction for energy conversion and storage: a comprehensive review, *Nano Energy* 37 (2017) 136–157, <https://doi.org/10.1016/j.nanoen.2017.05.022>.
- [11] M. Li, Y. Xiong, X. Liu, X. Bo, Y. Zhang, C. Han, L. Guo, Facile synthesis of electrospun MFe_2O_4 ($M = Co, Ni, Cu, Mn$) spinel nanofibers with excellent electrocatalytic properties for oxygen evolution and hydrogen peroxide reduction, *Nanoscale* 7 (2015) 8920–8930, <https://doi.org/10.1039/C4NR07243J>.
- [12] A. Kargar, S. Yavuz, T.K. Kim, C.-H. Liu, C. Kuru, C.S. Rustomji, S. Jin, P.R. Bandaru, Solution-processed $CoFe_2O_4$ nanoparticles on 3D carbon fiber papers for durable oxygen evolution reaction, *ACS Appl. Mater. Interfaces* 7 (2015) 17851–17856, <https://doi.org/10.1021/acsami.5b04270>.
- [13] Y. Xu, W. Bian, J. Wu, J.-H. Tian, R. Yang, Preparation and electrocatalytic activity of 3D hierarchical porous spinel $CoFe_2O_4$ hollow nanospheres as efficient catalyst for oxygen reduction reaction and oxygen evolution reaction, *Electrochim. Acta* 151 (2015) 276–283, <https://doi.org/10.1016/j.electacta.2014.11.042>.
- [14] L. Han, P. Tang, A. Reyes-Carmona, B. Rodríguez-García, M. Torrén, J.R. Morante, J. Arbiol, J.R. Galan-Mascaros, Enhanced activity and acid pH stability of prussian blue-type oxygen evolution electrocatalysts processed by chemical etching, *J. Am. Chem. Soc.* 138 (2016) 16037–16045, <https://doi.org/10.1021/jacs.6b09778>.
- [15] T. Li, Y. Lv, J. Su, Y. Wang, Q. Yang, Y. Zhang, J. Zhou, L. Xu, D. Sun, Y. Tang, Anchoring $CoFe_2O_4$ nanoparticles on N-doped carbon nanofibers for high-performance oxygen evolution reaction, *Adv. Sci.* 4 (2017) 1700226, , <https://doi.org/10.1002/advs.201700226>.
- [16] X. Lu, L. Gu, J. Wang, J. Wu, P. Liao, G. Li, Bimetal-organic framework derived $CoFe_2O_4/C$ porous hybrid nanorod arrays as high-performance electrocatalysts for oxygen evolution reaction, *Adv. Mater.* 29 (2017) 1604437, , <https://doi.org/10.1002/adma.201604437>.
- [17] W. Bian, Z. Yang, P. Strasser, R. Yang, A $CoFe_2O_4$ /graphene nanohybrid as an efficient bi-functional electrocatalyst for oxygen reduction and oxygen evolution, *J. Power Sources* 250 (2014) 196–203, <https://doi.org/10.1016/j.jpowsour.2013.11.024>.
- [18] X. Ji, S. Hao, F. Qu, J. Liu, G. Du, A.M. Asiri, L. Chen, X. Sun, Core-shell $CoFe_2O_4@Co-Fe-Bi$ nanoarray: a surface-amorphization water oxidation catalyst operating at near-neutral pH, *Nanoscale* 9 (2017) 7714–7718, <https://doi.org/10.1039/C7NR02929B>.
- [19] Y. Xu, X. Wang, H. Chen, D. Kuang, C. Su, Toward high performance photoelectrochemical water oxidation: combined effects of ultrafine cobalt iron oxide nanoparticle, *Adv. Funct. Mater.* 26 (2016) 4414–4421, <https://doi.org/10.1002/adfm.201600232>.
- [20] C. Singh, A. Goyal, S. Singhal, Nickel-doped cobalt ferrite nanoparticles: efficient catalysts for the reduction of nitroaromatic compounds and photo-oxidative degradation of toxic dyes, *Nanoscale* 6 (2014) 7959–7970, <https://doi.org/10.1039/C4NR01730G>.
- [21] A.J. Martín, G.O. Larrazábal, J. Pérez-Ramírez, Towards sustainable fuels and chemicals through the electrochemical reduction of CO_2 : lessons from water electrolysis, *Green Chem.* 17 (2015) 5114–5130, <https://doi.org/10.1039/C5GC01893E>.
- [22] P.K. Shen, C. Xu, Alcohol oxidation on nanocrystalline oxide Pd/C promoted electrocatalysts, *Electrochim. Commun.* 8 (2006) 184–188, <https://doi.org/10.1016/j.elecom.2005.11.013>.
- [23] G. Chen, Electrochemical technologies in wastewater treatment, *Sep. Purif. Technol.* 38 (2004) 11–41, <https://doi.org/10.1016/j.seppur.2003.10.006>.
- [24] K. Bouzek, M. Paidar, A. Sadilkova, H. Bergmann, Electrochemical reduction of nitrate in weakly alkaline solutions, *J. Appl. Electrochem.* 31 (2001) 1185–1193, <https://doi.org/10.1023/A:1012755222981>.
- [25] F. Urbain, V. Smirnov, J.-P. Becker, A. Lambertz, F. Yang, J. Ziegler, B. Kaiser, W. Jaegermann, U. Rau, F. Finger, Multijunction Si photocathodes with tunable photovoltages from 2.0 V to 2.8 V for light induced water splitting, *Energy Environ. Sci.* 9 (2016) 145–154, <https://doi.org/10.1039/C5EE02393A>.
- [26] A. Lambertz, F. Finger, R.E.I. Schropp, U. Rau, V. Smirnov, Preparation and measurement of highly efficient a-Si: H single junction solar cells and the advantages of $\mu c-SiO_x$: H n-layers, *Prog. Photovoltaics Res. Appl.* 23 (2015) 939–948, <https://doi.org/10.1002/pip.2629>.
- [27] A. Cabot, V.F. Puntes, E. Shevchenko, Y. Yin, L. Balcells, M.A. Marcus, S.M. Hughes, A.P. Alivisatos, Vacancy coalescence during oxidation of iron nanoparticles, *J. Am. Chem. Soc.* 129 (2007) 10358–10360, <https://doi.org/10.1021/ja072574a>.
- [28] A. Cabot, M. Ibáñez, P. Guardia, A.P. Alivisatos, Reaction regimes on the synthesis of hollow particles by the Kirkendall effect, *J. Am. Chem. Soc.* 131 (2009) 11326–11328, <https://doi.org/10.1021/ja903751p>.
- [29] M. Ibáñez, J. Fan, W. Li, D. Cadavid, R. Nafria, A. Carrete, A. Cabot, Means and limits of control of the shell parameters in hollow nanoparticles obtained by the Kirkendall effect, *Chem. Mater.* 23 (2011) 3095–3104, <https://doi.org/10.1021/cm2006633>.
- [30] T. Berestok, P. Guardia, J.B. Portals, S. Estradé, J. Llorca, F. Peiró, A. Cabot, S.L. Brock, Surface chemistry and nano-/microstructure engineering on photo-catalytic In_2S_3 nanocrystals, *Langmuir*. 34 (2018) 6470–6479, <https://doi.org/10.1021/acs.langmuir.8b00406>.

[31] T. Berestok, P. Guardia, M. Ibáñez, M. Meyns, M. Colombo, M.V. Kovalenko, F. Peiró, A. Cabot, Electrostatic-driven gelation of colloidal nanocrystals, *Langmuir* 34 (2018) 9167–9174, <https://doi.org/10.1021/acs.langmuir.8b01111>.

[32] T. Berestok, P. Guardia, R. Du, J.B. Portals, M. Colombo, S. Estradé, F. Peiró, S.L. Brock, A. Cabot, Metal oxide aerogels with controlled crystallinity and faceting from the epoxide-driven cross-linking of colloidal nanocrystals, *ACS Appl. Mater. Interfaces* 10 (2018) 16041–16048, <https://doi.org/10.1021/acsmami.8b03754>.

[33] Q.Q. Xiong, J.P. Tu, S.J. Shi, X.Y. Liu, X.L. Wang, C.D. Gu, Ascorbic acid-assisted synthesis of cobalt ferrite (CoFe_2O_4) hierarchical flower-like microspheres with enhanced lithium storage properties, *J. Power Sources* 256 (2014) 153–159, <https://doi.org/10.1016/j.jpowsour.2014.01.038>.

[34] J. Liu, R. Meng, J. Li, P. Jian, L. Wang, R. Jian, Achieving high-performance for catalytic epoxidation of styrene with uniform magnetically separable CoFe_2O_4 nanoparticles, *Appl. Catal. B Environ.* 254 (2019) 214–222, <https://doi.org/10.1016/j.apcatb.2019.04.083>.

[35] M. Zhang, X. Yang, X. Kan, X. Wang, L. Ma, M. Jia, Carbon-encapsulated CoFe_2O_4 /graphene nanocomposite as high performance anode for lithium ion batteries, *Electrochim. Acta* 112 (2013) 727–734, <https://doi.org/10.1016/j.electacta.2013.09.034>.

[36] P. Gründler, A. Kirbs, L. Dunsch, Modern thermoelectrochemistry, *ChemPhysChem* 10 (2009) 1722–1746, <https://doi.org/10.1002/cphc.200900254>.

[37] G.G. Wildgoose, D. Giovanelli, N.S. Lawrence, R.G. Compton, High-Temperature Electrochemistry: A Review, *Electroanal. Int. J. Devoted Fundam. Pract. Asp. Electroanal.* 16 (2004) 421–433, <https://doi.org/10.1002/elan.200302875>.

[38] F. Urbain, J.-P. Becker, V. Smirnov, J. Ziegler, F. Yang, B. Kaiser, W. Jaegermann, S. Hoch, A. Maljusch, U. Rau, F. Finger, Influence of the operating temperature on the performance of silicon based photoelectrochemical devices for water splitting, *Mater. Sci. Semicond. Process.* 42 (2016) 142–146, <https://doi.org/10.1016/j.mssp.2015.08.045>.

[39] S. Klaus, Y. Cai, M.W. Louie, L. Trotochaud, A.T. Bell, Effects of Fe electrolyte impurities on $\text{Ni}(\text{OH})_2/\text{NiOOH}$ structure and oxygen evolution activity, *J. Phys. Chem. C* 119 (2015) 7243–7254, <https://doi.org/10.1021/acs.jpcc.5b00105>.

[40] F. Urbain, P. Tang, N.M. Carretero, T. Andreu, J. Arbiol, J.R. Morante, Tailoring copper foam with silver dendrite catalysts for highly selective carbon dioxide conversion into carbon monoxide, *ACS Appl. Mater. Interfaces* 10 (2018) 43650–43660, <https://doi.org/10.1021/acsami.8b15379>.

[41] F. Urbain, P. Tang, N.M. Carretero, T. Andreu, L.G. Gerling, C. Voz, J. Arbiol, J.R. Morante, A prototype reactor for highly selective solar-driven CO_2 reduction to synthesis gas using nanosized earth-abundant catalysts and silicon photovoltaics, *Energy Environ. Sci.* 10 (2017) 2256–2266, <https://doi.org/10.1039/C7EE01747B>.

[42] E. Irtem, T. Andreu, A. Parra, M.D. Hernández-Alonso, S. García-Rodríguez, J.M. Riesco-García, G. Penelas-Pérez, J.R. Morante, Low-energy formate production from CO_2 electroreduction using electrodeposited tin on GDE, *J. Mater. Chem. A* 4 (2016) 13582–13588, <https://doi.org/10.1039/C6TA04432H>.

[43] M.D.H. ALONSO, G.P. PÉREZ, T. Andreu, E. Irtem, A. Parra, C. Fábregas, J.R. Morante, Filter-press Photoelectrochemical Water Oxidation and CO_2 Reduction Cell, (2018).

[44] Q. Ma, M. Li, L. Pang, X. Ren, C. Li, X. Xu, S. Liu, Solar-to-hydrogen efficiency of 9.5% by using a thin-layer platinum catalyst and commercial amorphous silicon solar cells, *ChemCatChem* 8 (2016) 1713–1717, <https://doi.org/10.1002/cctc.201600170>.

[45] C. Trompoukis, A. Abass, J.-W. Schüttauf, T. Bosserez, J. Rongé, J. Lauwaert, J.A. Martens, R. Baets, Porous multi-junction thin-film silicon solar cells for scalable solar water splitting, *Sol. Energy Mater. Sol. Cells* 182 (2018) 196–203, <https://doi.org/10.1016/j.solmat.2018.03.041>.

[46] Y. Tan, H. Wang, P. Liu, Y. Shen, C. Cheng, A. Hirata, T. Fujita, Z. Tang, M. Chen, Versatile nanoporous bimetallic phosphides towards electrochemical water splitting, *Energy Environ. Sci.* 9 (2016) 2257–2261, <https://doi.org/10.1039/C6EE01109H>.

[47] N. Jiang, B. You, M. Sheng, Y. Sun, Electrodeposited cobalt-phosphorous-derived films as competent bifunctional catalysts for overall water splitting, *Angew. Chem. Int. Ed.* 54 (2015) 6251–6254, <https://doi.org/10.1002/anie.201501616>.

[48] J. Jia, L.C. Seitz, J.D. Benck, Y. Huo, Y. Chen, J.W.D. Ng, T. Bilir, J.S. Harris, T.F. Jaramillo, Solar water splitting by photovoltaic-electrolysis with a solar-to-hydrogen efficiency over 30%, *Nat. Commun.* 7 (2016) 13237, <https://doi.org/10.1038/ncomms13237>.

[49] F. Urbain, P. Tang, V. Smirnov, K. Welter, T. Andreu, F. Finger, J. Arbiol, J.R. Morante, Multilayered hematite nanowires with thin-film silicon photovoltaics in an all-earth-abundant hybrid tandem device for solar water splitting, *ChemSusChem* 12 (2019) 1428–1436, <https://doi.org/10.1002/cssc.201802845>.

[50] B.M. Klahr, D. Peterson, K. Randolph, E.L. Miller, Innovative approaches to addressing the fundamental materials challenges in advanced water splitting technologies for renewable hydrogen production, *ECS Trans.* 75 (2017) 3–11, <https://doi.org/10.1149/07550.0003ecst>.

[51] J.H. Montoya, L.C. Seitz, P. Chakhranont, A. Vojvodic, T.F. Jaramillo, J.K. Nørskov, Materials for solar fuels and chemicals, *Nat. Mater.* 16 (2017) 70, <https://doi.org/10.1038/nmat4778>.

Further reading

S.H. Joo, S.J. Choi, I. Oh, J. Kwak, Z. Liu, O. Terasaki, R. Ryoo, Ordered nanoporous arrays of carbon supporting high dispersions of platinum nanoparticles, *Nature* 2001; 412: 169–172. doi:10.1038/35084046.